Using Direct Laboratory Measurements of Electron Temperature Anisotropy to Identify the Heating Mechanism in Electron-Only Guide Field Magnetic Reconnection

Peiyun Shi,[1,2,*] Earl E. Scime,[1,†] M. Hasan Barbhuiya,[1] Paul A. Cassak,[1] Subash Adhikari,[1] M. Swisdak,[3] and Julia E. Stawarz[4]

[1]*Department of Physics and Astronomy and the Center for KINETIC Plasma Physics, West Virginia University, Morgantown, West Virginia 26506, USA*

[2]*Princeton Plasma Physics Laboratory, Princeton, New Jersey 08542, USA*

[3]*Institute for Research in Electronics and Applied Physics, University of Maryland, College Park, Maryland 20742, USA*

[4]*Department of Mathematics, Physics, and Electrical Engineering, Northumbria University, Newcastle upon Tyne NE1 8ST, United Kingdom*

(Received 31 March 2023; revised 21 July 2023; accepted 12 September 2023; published 10 October 2023)

Anisotropic electron heating during electron-only magnetic reconnection with a large guide magnetic field is directly measured in a laboratory plasma through *in situ* measurements of electron velocity distribution functions. Electron heating preferentially parallel to the magnetic field is localized to one separatrix, and anisotropies of 1.5 are measured. The mechanism for electron energization is identified as the parallel reconnection electric field because of the anisotropic nature of the heating and spatial localization. These characteristics are reproduced in a 2D particle-in-cell simulation and are also consistent with numerous magnetosheath observations. A measured increase in the perpendicular temperature along both separatrices is not reproduced by our 2D simulations. This work has implications for energy partition studies in magnetosheath and laboratory reconnection.

DOI: 10.1103/PhysRevLett.131.155101

Introduction.—Magnetic reconnection, which reconfigures the magnetic field and converts stored magnetic energy into thermal, kinetic, and nonthermal energy of particles [1–3], is an important particle acceleration mechanism in magnetized plasmas. In the solar corona, electrons accelerated during reconnection generate the hard x-ray emission observed above coronal loops associated with solar flares [4,5]. In Earth's magnetotail, electrons are energized up to ∼300 keV inside the diffusion region during reconnection [6]. In laboratory fusion plasmas, bulk electron temperatures above 1 keV and superthermal electrons up to 100 keV are observed during the merging of two spheromak plasmas [7] and during sawtooth instabilities in tokamaks [8,9].

Some processes potentially responsible for electron energization during reconnection are identifiable by the directionality of the energization relative to the magnetic field **B**. Fermi acceleration of electrons in the parallel direction occurs in high **B**-curvature regions [10–12] while the betatron mechanism energizes electrons in the perpendicular direction in regions of strong **B** gradients [13]. When there is a large out-of-plane (guide) magnetic field B_g, simulations reveal that perpendicular electron heating tends to be quenched [14,15], and parallel electron heating results from energization by the reconnection electric field E_{rec} that is nearly parallel to the local **B** [16]. Regardless of the acceleration mechanism, converting the energy associated with particle acceleration into thermal energy mainly requires additional velocity space scattering processes, e.g., Coulomb collisions or wave-particle interactions [17].

Consistent with theoretical predictions, primarily parallel electron heating was observed during reconnection with large B_g in Earth's turbulent magnetosheath [18–21]. A drawback of satellite observations is that they are made along a small number of trajectories. So while they can be effective at revealing local physics, it is challenging to extract information about 2D and 3D reconnection structures [22,23]. Such structures can be measured in laboratory experiments [24–26]. The generation of nonthermal electrons possibly accelerated by E_{rec} was measured in a reconnecting laser plasma [27]. Only high-energy tails of electron velocity distribution functions (EVDFs) were measured *ex situ* in that experiment. No systematic *in situ* measurements of EVDFs along multiple velocity directions or their spatial distribution have been reported. Such measurements are critical to the identification of mechanisms responsible for electron energization [3,28,29].

A regime of reconnection, called electron-only reconnection since there is insufficient time or space for ions to couple with reconnection structures [30–32], provides an opportunity to study electron heating mechanisms more directly than in fully ion-coupled reconnection. Electron-only reconnection is thought to be important for energy dissipation at kinetic scales in Earth's turbulent magnetosheath [20,33–36], bow shock [37,38], and the quiet

magnetotail [39,40]. Recent simulations of turbulent near-Sun plasmas [41] suggest that electron-only reconnection with a large B_g plays a key role in the dissipation of turbulent energy at the kinetic scale and results in parallel, i.e., anisotropic, electron heating.

In this Letter, we present direct *in situ* measurements of both perpendicular $T_{e\perp}$ and parallel $T_{e\parallel}$ electron temperature (relative to the local **B**) and their spatial distribution in the reconnection plane during electron-only reconnection in a laboratory plasma. Parallel electron heating dominates over perpendicular heating along one separatrix, with the electron temperature anisotropy $T_{e\parallel}/T_{e\perp}$ reaching 1.5. The preferential parallel electron heating and its spatial localization are reproduced in our 2D particle-in-cell (PIC) simulations, which leads us to conclude that electron energization by reconnection electric field E_{rec} ($\parallel$ to **B** when B_g is large) is responsible for the observed electron heating in our experiments. These observations are consistent with previous experimental studies that were unable to directly measure temperature anisotropies or their spatial distribution during ion-coupled, modest-B_g reconnection [24]. Significant perpendicular electron heating also appears along both separatrices and increases with distance from the X point, a phenomenon not reproduced in simulations. This result highlights the necessity of measuring multidimensional EVDFs to determine the full energy budget of reconnection in laboratory and magnetosheath plasmas.

Experimental setup and temperature measurement.—Figure 1(a) shows the experimental configuration in the linear PHAse Space MApping (PHASMA) device [42]. Two magnetized argon flux ropes are launched by drawing axial current along two plasma columns, separated by $\Delta = 60$ mm along the x direction [32,43–45]. Magnetic reconnection is driven by the interaction between the two flux ropes, i.e., they merge and bounce [46–48]. The reconnection is firmly in the electron-only regime because the reconnection duration 20 μs is smaller than one ion gyroperiod $\tau_{ci} \sim 70$ μs and because Δ is roughly $1.5\rho_s$, where ρ_s is the ion gyroradius based on the ion sound speed [32,49–51]. Such a system size is much smaller than the tens of ρ_s required for ion-coupled reconnection [31,52].

To maximize the available reconnection magnetic energy and experimental repeatability, we create flux ropes with currents above the threshold of the $m = 1$ kink instability [42] but with a discharge period less than one axial Alfvén time so that kink fluctuations do not have enough time to grow [48]. Representative in-plane projections of magnetic field lines measured by magnetic probes are plotted as black lines in the inset of Fig. 1(a), showing the typical X-type reconnection geometry [53–56] with two separatrices denoted by red and blue dashed lines.

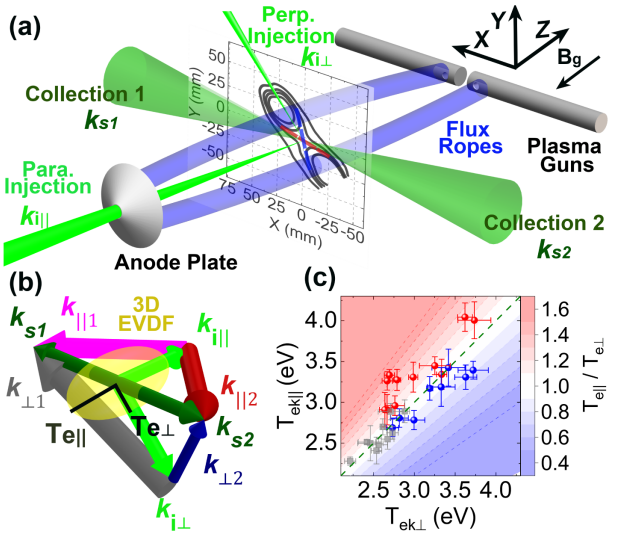

FIG. 1. (a) PHASMA creates two interacting magnetic flux ropes (blue) with plasma guns and an anode (gray). In-plane magnetic field projections (black lines) during pull reconnection [32] are plotted in the inset. Red and blue dashed lines denote separatrix I and II, respectively. The 3D Thomson scattering system includes two injection beams (along perpendicular $\mathbf{k_{i\perp}}$ and parallel $\mathbf{k_{i\parallel}}$ directions) in light green and two collection optics (along $\mathbf{k_{s1}}$ and $\mathbf{k_{s2}}$) in dark green. (b) An anisotropic EVDF (yellow) for gyrotropic electrons with different perpendicular and parallel temperatures ($T_{e\perp}$ and $T_{e\parallel}$) is measured along four wave vectors, $\mathbf{k_{\perp 1}}$, $\mathbf{k_{\perp 2}}$, $\mathbf{k_{\parallel 1}}$ and $\mathbf{k_{\parallel 2}}$. (c) Measured electron temperatures $T_{ek\perp}$ and $T_{ek\parallel}$ around two separatrices (red and blue circles for separatrix I and II, respectively) and the inflow region (gray squares). The background color is $T_{e\parallel}/T_{e\perp}$.

The electron temperature anisotropy is measured with multidimensional incoherent Thomson scattering [57] with the spatial resolution $\lesssim 1$ mm in the absence of magnetic probes. In addition to perpendicular injection of laser light along $\mathbf{k_{i\perp}}$ and collection along $\mathbf{k_{s1}}$ [see Fig. 1(a)] [58], a parallel injection beam path along $\mathbf{k_{i\parallel}}$ and collection along $\mathbf{k_{s2}}$ have been added to enable measuring multidimensional EVDFs. Thomson scattering produces EVDFs in the directions of the differences between all of the collection and injection directions, namely $\mathbf{k_{\perp 1}} = \mathbf{k_{s1}} - \mathbf{k_{i\perp}}$, $\mathbf{k_{\perp 2}} = \mathbf{k_{s2}} - \mathbf{k_{i\perp}}$, $\mathbf{k_{\parallel 1}} = \mathbf{k_{s1}} - \mathbf{k_{i\parallel}}$, and $\mathbf{k_{\parallel 2}} = \mathbf{k_{s2}} - \mathbf{k_{i\parallel}}$, as are sketched in Fig. 1(b), along with a yellow ellipse representing an idealized gyrotropic EVDF $f_e(v_\perp, v_\parallel)$ with different $T_{e\perp}$ and $T_{e\parallel}$. We define the 1D EVDFs in the measurement directions as $f_e(v_{k\perp 1})$, $f_e(v_{k\perp 2})$, $f_e(v_{k\parallel 1})$, and $f_e(v_{k\parallel 2})$, and the associated electron temperatures in each direction as $T_{ek\perp 1}$, $T_{ek\perp 2}$, $T_{ek\parallel 1}$, and $T_{ek\parallel 2}$, respectively. Since the electrons are strongly magnetized in this experiment, we expect them to be gyrotropic, i.e., $T_{ek\perp 1} = T_{ek\perp 2}$, which we define as $T_{ek\perp}$. Since $\mathbf{k_{\parallel 1}}$ and $\mathbf{k_{\parallel 2}}$ are constructed to be symmetric about the parallel direction ($\pm 45°$), $T_{ek\parallel 1} = T_{ek\parallel 2}$, which we define as $T_{ek\parallel}$. From the geometry of the

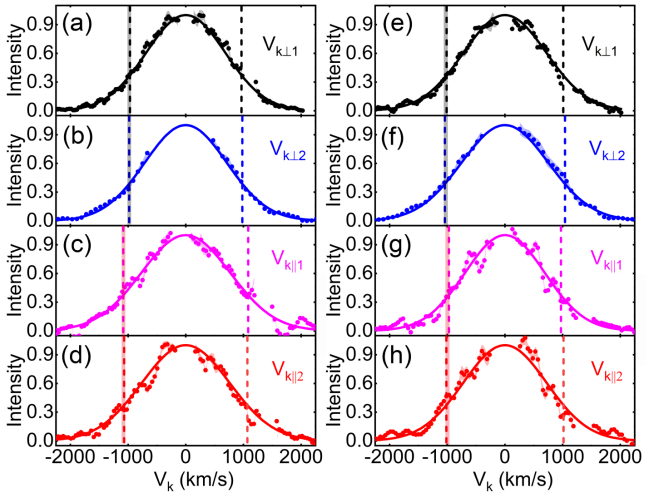

FIG. 2. Measured EVDFs around separatrix I [the red dashed line in Fig. 1(a)]: (a) $f_e(v_{k\perp1})$, (b) $f_e(v_{k\perp2})$, (c) $f_e(v_{k\parallel1})$, and (d) $f_e(v_{k\parallel2})$. Vertical dashed lines denote electron thermal velocities calculated from Maxwellian fits to the EVDFs (dotted lines). Semitransparent vertical black and red bars show the electron thermal velocities for $T_{ek\perp}$ and $T_{ek\parallel}$. (e)–(h) Similar to (a)–(d), but measured around separatrix II [blue dashed line in Fig. 1(a)]. Anisotropy is the difference between $T_{ek\perp}$ and $T_{ek\parallel}$ in (a)–(d).

distribution, the perpendicular electron temperature $T_{e\perp}$ is equal to $T_{ek\perp}$. The parallel electron temperature, derived in the Supplemental Material [59], is

$$T_{e\parallel} = 2T_{ek\parallel} - T_{ek\perp}. \quad (1)$$

Results.—Figure 1(c) briefly summarizes the measured $T_{ek\perp}$ and $T_{ek\parallel}$ at different locations, with the background shading showing electron temperature anisotropy $T_{e\parallel}/T_{e\perp}$ during the pull phase of electron-only reconnection [48]. Around separatrix I, denoted by the red dashed line in Fig. 1(a), $T_{e\parallel}/T_{e\perp}$ (red circles) is considerably larger than 1, with a mean value of 1.3 and a standard deviation of 0.2. Along separatrix II, $T_{e\parallel}/T_{e\perp}$ (blue circles) is ~1, with a mean value of 0.92 and a standard deviation of 0.08. This difference from unity is not statistically significant. In comparison, $T_{e\parallel}/T_{e\perp}$ in the inflow region (gray squares) is close to 1, with a mean value of 1.0 and a standard deviation of 0.08. Thus, the electron temperature along separatrix I is significantly anisotropic, but not along separatrix II.

Typical EVDF measurements $f_e(v_{k\perp1})$, $f_e(v_{k\perp2})$, $f_e(v_{k\parallel1})$, and $f_e(v_{k\parallel2})$ at $(x, y) = (-5\text{ mm}, -7\text{ mm})$ around separatrix I are presented in Figs. 2(a)–2(d) and at $(x, y) = (7\text{ mm}, 0\text{ mm})$ around separatrix II in Figs. 2(e) and 2(f). Each raw Thomson scattering spectrum is separately measured by accumulating 35 reproducible experimental shots and is well fit with single Maxwellian EVDFs (solid lines). The vertical dashed lines are the thermal speeds from the fits. The different velocity resolutions arise from the different magnitudes of $\mathbf{k}_{\perp1}$, $\mathbf{k}_{\perp2}$, $\mathbf{k}_{\parallel1}$, and $\mathbf{k}_{\parallel2}$ in Fig. 1(b). The cutoff region around 0 km/s in the EVDFs is due to optical filters used to reject stray light at the laser wavelength [58]. Some data points around the velocity corresponding to 528.5 nm are also excluded from the fits because there is strong emission from an impurity Fe I line. As expected for strongly magnetized electrons, the spectral widths at separatrix I of $f_e(v_{k\perp1})$ and $f_e(v_{k\parallel1})$ are approximately equal to those of $f_e(v_{k\perp2})$ and $f_e(v_{k\parallel2})$, respectively, i.e., $T_{ek\perp1} \approx T_{ek\perp2} = T_{ek\perp}$ and $T_{ek\parallel1} \approx T_{ek\parallel2} = T_{ek\parallel}$. Notably, these two directly measured temperatures $T_{ek\perp} = 2.7 \pm 0.1$ eV and $T_{ek\parallel} = 3.3 \pm 0.1$ eV are different enough that there is a significant electron temperature anisotropy.

Using Eq. (1), $T_{e\parallel}$ is 4.0 ± 0.2 eV. With $T_{e\perp} = 2.7 \pm 0.1$ eV, the electron temperature measurements around separatrix I are clearly anisotropic, indicating preferential parallel electron heating. The electron temperature anisotropy $T_{e\parallel}/T_{e\perp} = 1.5 \pm 0.1$. Around separatrix II, $T_{ek\parallel} = 2.8 \pm 0.1$ eV is within measurement uncertainty of $T_{ek\perp} = T_{e\perp} = 3.0 \pm 0.2$ eV. Thus, $T_{e\parallel} = 2.6 \pm 0.2$ eV, $T_{e\parallel}/T_{e\perp} = 0.9 \pm 0.1$, and the electron temperatures around separatrix II are not significantly anisotropic.

Note that electrons both in upstream regions [gray squares in Fig. 1(c)] and in single flux ropes (see the Supplemental Material [59]) are measured to be nearly isotropic. Therefore, the observed electron temperature anisotropy around separatrix I is strong evidence of electron heating resulting from guide field reconnection, consistent with theoretical predictions that a quadrupolar electron pressure profile arises in order to maintain pressure balance when the quadrupolar Hall magnetic field is superposed with B_g [24,49,51,64].

To investigate the nature of the anisotropic electron energization, $T_{ek\perp}$ and $T_{ek\parallel}$ are measured throughout the reconnection plane. Figures 3(a)–3(d) show measurements at 43 spatial locations [black circles in (a)] that cover most of the electron diffusion region including both separatrices and one inflow region. At each measurement location, $T_{e\perp}$ and $T_{e\parallel}$ are derived and plotted in Figs. 3(a) and 3(b). The effective electron temperature, $T_e = (2T_{e\perp} + T_{e\parallel})/3$, and electron temperature anisotropy $T_{e\parallel}/T_{e\perp}$ are shown in Figs. 3(c) and 3(d). Clearly, anisotropic heating ($T_{e\parallel}/T_{e\perp} > 1$) occurs around only separatrix I [red dashed line in Fig. 3(d)]. Along separatrix II, there is a very weak anisotropy, if any, i.e., $T_{e\parallel}/T_{e\perp}$ is slightly smaller than 1 but within the measurement uncertainty of being isotropic.

The corresponding 1D profiles of $T_{e\perp}$, $T_{e\parallel}$, T_e, and $T_{e\parallel}/T_{e\perp}$ along separatrix I (red points), II (blue squares), and the inflow (black open squares) directions [indicated by red, blue, and black dashed lines in Fig. 3(d)] are presented in Figs. 3(e)–3(h) for quantitative analysis. For comparison, the upstream electrons have $T_e = 2.6$ eV. The monotonically increasing T_e increment, $\Delta T_{e\parallel}$, reaches 1.4 eV along separatrix I, whereas $T_{e\parallel}$ decreases within 5 mm from the

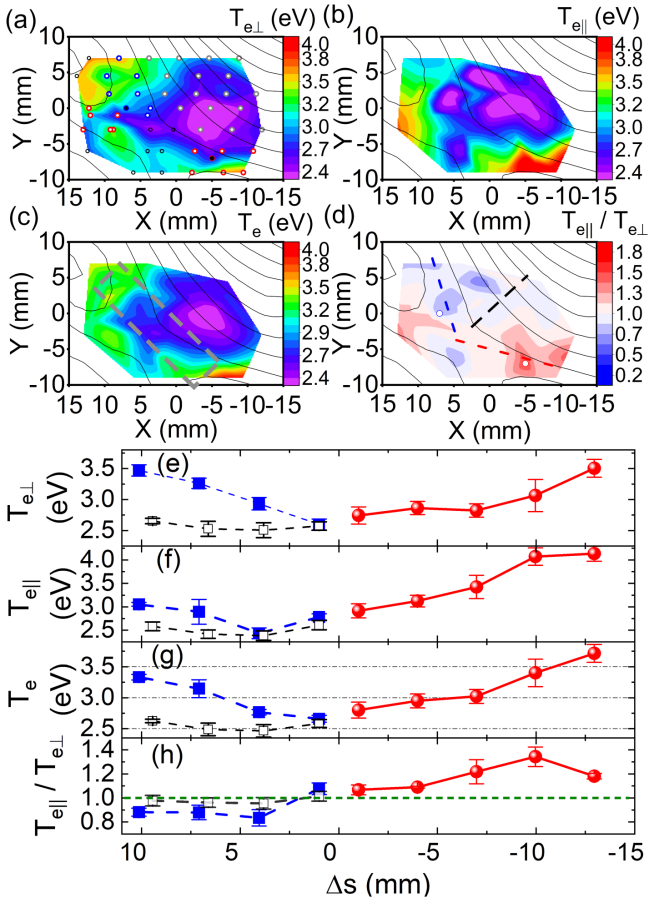

FIG. 3. 2D spatial profile of (a) perpendicular electron temperature $T_{e\perp}$, (b) parallel electron temperature $T_{e\parallel}$, (c) effective electron temperature T_e and (d) anisotropy $T_{e\parallel}/T_{e\perp}$. Black lines are in-plane magnetic field projections, and 43 dots show the measurement locations, grouped into regions around the separatrix I (red), II (blue), and the inflow (gray). The dashed rectangle in (c), half of the electron diffusion region, is used to calculate energy fluxes. The corresponding 1D profiles along separatrix I [red points for the red dashed line in (d)], II [blue solid squares for the blue dashed line in (d)] and the inflow direction [black open squares for the black dashed line in (d)]: (e) $T_{e\perp}$, (f) $T_{e\parallel}$, (g) T_e, and (h) $T_{e\parallel}/T_{e\perp}$. Δs is the distance from the X point at $(x, y) = (5\ \text{mm}, -3\ \text{mm})$.

X point, $(x, y) = (5\ \text{mm}, -3\ \text{mm})$, along separatrix II before later increasing by 0.5 eV further downstream. Monotonic increases of $T_{e\perp}$ and T_e are measured along both separatrices.

Discussion.—To identify the electron energization mechanism responsible for the heating, we estimate the energy gain rate from different mechanisms. For Fermi acceleration, electrons gain energy density $W_\parallel$ preferentially along the parallel direction at a rate $\dot{W}_\parallel = (n_e k_B T_{e\parallel}/\tau_{\text{rec}}) \times [1/(1 + 2(B_g/B_{\text{rec}})^2)] \sim 0.04\ \text{W/cm}^3$ [10,16,65], where the electron density $n_e = 1 \times 10^{19}\ \text{m}^{-3}$, reconnection magnetic field $B_{\text{rec}} = 15$ G, k_B is the Boltzmann constant, reconnection time τ_{rec} is defined as electron transit time to cross current sheet thickness, and the last term is the dependence on magnetic field curvature. In betatron acceleration [13], the perpendicular electron energy density $W_\perp$ increases at a rate $\dot{W}_\perp = (n_e k_B T_{e\perp}/\tau_{\text{rec}}) \cdot (B_{\text{rec}}/B_g)^2 \cdot (\delta/L)^2 \sim 0.02\ \text{W/cm}^3$ (see derivations in the Supplemental Material [59]), where δ and L are the thickness and length of the electron diffusion region. However, the measured electron energy density gain rate $n_e k_B \Delta T_e/\tau_{\text{rec}} \sim 4\ \text{W/cm}^3$ is too large to be caused by either the Fermi or betatron mechanisms.

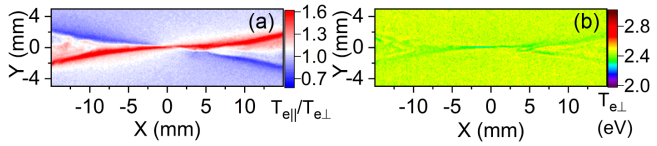

FIG. 4. (a) $T_{e\parallel}/T_{e\perp}$ and (b) $T_{e\perp}$ in the reconnection plane obtained from a 2D PIC simulation.

In contrast, the energy density gain rate from the parallel reconnection electric field $E_\parallel$ is $E_\parallel j_\parallel = E_{\text{rec}} j_{\text{rec}} \sim 3\ \text{W/cm}^3$, where E_{rec} is nearly parallel to the magnetic field for $B_g \gg B_{\text{rec}}$, and $E_{\text{rec}} \approx 0.1 c_{Ae} B_{\text{rec}}$, assuming a normalized reconnection rate of 0.1 [31,66–69], c_{Ae} is the electron Alfvén velocity based on B_{rec} [16,24,30], and $j_{\text{rec}} = 5\ \text{A/cm}^2$ is the axial current density near the X point. Note that electron heat losses due to axial advection, axial conduction, and radiation are approximately 1 order of magnitude smaller than $E_{\parallel j\parallel}$ and do not play a significant role in the observed electron energization. Therefore, acceleration by E_{rec} is likely the major contributor to electron energization in our experiment. Preferential parallel electron heating during reconnection with large B_g is consistent with magnetosheath observations [18–21] and a recent spheromak-merging experiment [70].

We compare these results to a 2D PIC simulation for our experimental conditions, as described in the Supplemental Material [59]. The current sheet in the simulation has its guide field aligned with the initial current, as in the experiment. As is shown in Fig. 4(a), the simulated electron temperature anisotropy reaches $T_{e\parallel}/T_{e\perp} \sim 1.6$ and is localized around separatrix I, which agrees well with the experiment. The energy density gain rate $E_{\parallel j\parallel} \sim 20\ \text{W/cm}^3$ is 2 orders of magnitude larger than that arising from Fermi and betatron acceleration, supporting the conclusion that the nearly parallel E_{rec} is the major driver of anisotropic electron heating, consistent with previous numerical simulations [14–16]. No $T_{e\perp}$ enhancement around either separatrix is observed in this 2D simulation, as shown in Fig. 4(b).

There are different possible velocity space scattering processes that could convert directed (parallel) electron energy into thermal energy ($T_{e\parallel}$ and $T_{e\perp}$). Phase mixing has been proposed for preferential parallel heating around a separatrix in large-B_g, low-β reconnection plasmas [17] like

PHASMA. This process requires that electrons streaming along $\mathbf{B}$ with speed $v_{e\parallel}$ resonate with the electromagnetic field that develops at speed c_{Ae} in the reconnection plane [71]. But $v_{e\parallel}(B_{\rm rec}/B_g) \sim 40\,{\rm km/s} \ll c_{Ae} \sim 400\,{\rm km/s}$ in the experiment, where $v_{e\parallel}$ is the electron thermal speed, so the required Landau resonance condition is not satisfied. The measured levels of anisotropy are insufficient to trigger electron firehose instabilities, $n_e k_B(T_{e\parallel} - T_{e\perp}) < B^2/2\mu_0$ [72,73], where μ_0 is the vacuum permeability. The absence of the firehose instability and the existence of a strong guide field means that a newly identified kinetic regime of reconnection with strong electron temperature anisotropy [74] due to electron trapping [75,76] is also unlikely to play a role in the conversion of parallel electron acceleration into heat in our experiment.

Although marginal collisionality is satisfied in the 2D reconnection plane, i.e., the mean free path of Coulomb collisions $\lambda_{\rm mfp} \approx 13$ mm $\sim 2.6\delta$, collisions are not ignorable for electrons transported long distances $(10\delta - 200\delta)$ along the axial direction z. Electrons in the outflow region flowing along the strong guide field continuously collisionally relax toward isotropy. Anisotropic temperatures are sustained for locally heated electrons along separatrix I because the collisional isotropization rate $-(T_{e\parallel} - T_e)/\tau_{\rm iso} \sim -20\,{\rm eV/\mu s}$, where $\tau_{]\rm iso}$ is the isotropization time [77], is smaller than the anisotropic heating rate due to reconnection, i.e., $\sim +30$ eV/μs, assuming only $T_{e\parallel}$ increases (see the Supplemental Material [59]). Without active anisotropic heating along separatrix II, the electron temperature relaxes to isotropy on a timescale of $\tau_{\rm iso} \sim 0.03\ \mu{\rm s} < \tau_{\rm rec}$.

The observed increase of $T_{e\perp}$ with distance from the X point along both separatrices could result from collisional isotropization of electrons that have undergone parallel electron heating (which increases with distance from the X point) flowing along the guide field. Transport across B_g is constrained by the small electron gyroradius, so where the parallel heating occurs in the region around the X point defines the spatial distribution of the total electron heating as well. For future work, we will explore electron heating throughout the outflow region through the 3D PIC simulations like those in Refs. [78–81] that include realistic collision rates and in laboratory experiments in which the overall level of collisionality, including electron-neutral contributions, is varied.

A key aspect of having measurements of parallel and perpendicular temperatures is a more accurate accounting of the energy budget during reconnection than has been done previously [32,82,83]. The electron flow speed obtained from fits to the EVDFs measured here is smaller than the measurement uncertainty of ±100 km/s. Given this measurement resolution, the upper limit on the electron flow kinetic energy is 3% of the incoming reconnection magnetic enthalpy and is ignorable in the energy partition calculation. The rectangular boundary of thickness $\delta = 5$ mm and length $2L = 20$ mm around the X point in Fig. 3(c) is used to calculate total electron enthalpy per unit axial length. The ratio of the increase of electron enthalpy from the inflow-side edge to the outflow-side edges to the incoming magnetic enthalpy is around 1. In other words, far from the X point, 100% of the available magnetic field energy ends up in electron thermal energy. For the central half-rectangular boundary with $\Delta s < 5$ mm, this ratio drops to 45%. Therefore, additional electron heating occurs beyond 5 mm from the X point. Possible heating mechanisms are the thermalization of electron flows in the outflow region and compressional heating as the outflow runs into the flux ropes, analogous to heating at dipolarization fronts in Earth's magnetotail [84–87].

We acknowledge fruitful discussion with Jan Egedal and technical assistance from Prabhakar Srivastav, Sonu Yadav, and Thomas Steinberger. This work was supported by NSF PHY Grants No. 1804428, No. 1827325, No. 1902111, and No. 2109083; NASA Grants No. 80NSSC19M0146 and No. 80NNSC22K0323; DoE No. DE-SC0020294; and the Royal Society University Research Fellowship No. URF\R1 \201286. This research uses resources of NERSC, a DOE Office of Science User Facility supported by the Office of Science under Contracts No. DE-AC02-05CH11231 and No. DE-AC02-09CH11466.

*pshi@pppl.gov
†earl.scime@mail.wvu.edu

[1] M. Yamada, R. Kulsrud, and H. Ji, Rev. Mod. Phys. **82**, 603 (2010).
[2] M. Hesse and P. A. Cassak, J. Geophys. Res. **125**, e2018JA025935 (2020).
[3] H. Ji, W. Daughton, J. Jara-Almonte, A. Le, A. Stanier, and J. Yoo, Nat. Rev. Phys. **4**, 263 (2022).
[4] S. Krucker, H. S. Hudson, L. Glesener, S. M. White, S. Masuda, J.-P. Wuelser, and R. P. Lin, Astrophys. J. **714**, 1108 (2010).
[5] G. D. Fleishman, G. M. Nita, B. Chen, S. Yu, and D. E. Gary, Nature (London) **606**, 674 (2022).
[6] M. Oieroset, R. P. Lin, T. D. Phan, D. E. Larson, S. D. Bale, and A. Szabo, Phys. Rev. Lett. **89**, 195001 (2002).
[7] T. Yamada, H. Tanabe, T. G. Watanabe, Y. Hayashi, R. Imazawa, M. Inomoto, Y. Ono, M. Gryaznevich, R. Scannell, and C. Michael, Nucl. Fusion **56**, 106019 (2016).
[8] P. V. Savrukhin, Phys. Rev. Lett. **86**, 3036 (2001).
[9] A. M. DuBois, A. F. Almagri, J. K. Anderson, D. J. Den Hartog, J. D. Lee, and J. S. Sarff, Phys. Rev. Lett. **118**, 075001 (2017).
[10] J. F. Drake, M. Swisdak, H. Che, and M. A. Shay, Nature (London) **443**, 553 (2006).
[11] F. Guo, H. Li, W. Daughton, and Y.-H. Liu, Phys. Rev. Lett. **113**, 155005 (2014).
[12] J. T. Dahlin, J. F. Drake, and M. Swisdak, Phys. Plasmas **21**, 092304 (2014).

[13] M. Hoshino, T. Mukai, T. Terasawa, and I. Shinohara, J. Geophys. Res. **106**, 25979 (2001).
[14] M. A. Shay, C. C. Haggerty, T. D. Phan, J. F. Drake, P. A. Cassak, P. Wu, M. Oieroset, M. Swisdak, and K. Malakit, Phys. Plasmas **21**, 122902 (2014).
[15] H. Wang, Q. Lu, C. Huang, and S. Wang, Phys. Plasmas **24**, 52113 (2017).
[16] J. T. Dahlin, J. F. Drake, and M. Swisdak, Phys. Plasmas **23**, 120704 (2016).
[17] N. F. Loureiro, A. A. Schekochihin, and A. Zocco, Phys. Rev. Lett. **111**, 025002 (2013).
[18] F. D. Wilder *et al.*, J. Geophys. Res. **123**, 6533 (2018).
[19] T. D. Phan, M. A. Shay, J. T. Gosling, M. Fujimoto, J. F. Drake, G. Paschmann, M. Oieroset, J. P. Eastwood, and V. Angelopoulos, Geophys. Res. Lett. **40**, 4475 (2013).
[20] J. E. Stawarz, J. P. Eastwood, T. D. Phan, I. L. Gingell, P. S. Pyakurel, M. A. Shay, S. L. Robertson, C. T. Russell, and O. Le Contel, Phys. Plasmas **29**, 012302 (2022).
[21] Q. Xu, M. Zhou, W. Ma, J. He, S. Huang, Z. Zhong, Y. Pang, and X. Deng, Authorea Preprints, 10.22541/essoar.167117460.01331212/v1 (2022).
[22] R. E. Ergun *et al.*, J. Geophys. Res. **124**, 10104 (2019).
[23] J. M. Schroeder, J. Egedal, G. Cozzani, Y. V. Khotyaintsev, W. Daughton, R. E. Denton, and J. L. Burch, Geophys. Res. Lett. **49**, e2022GL100384 (2022).
[24] W. Fox, F. Sciortino, A. v. Stechow, J. Jara-Almonte, J. Yoo, H. Ji, and M. Yamada, Phys. Rev. Lett. **118**, 125002 (2017).
[25] Y. Liu, P. Shi, X. Zhang, J. Lei, and W. Ding, Rev. Sci. Instrum. **92**, 71101 (2021).
[26] G. G. Howes, Phys. Plasmas **25**, 055501 (2018).
[27] A. Chien *et al.*, Nat. Phys. **19**, 254 (2023).
[28] J. T. Dahlin, Phys. Plasmas **27**, 100601 (2020).
[29] X. Li, F. Guo, and Y.-H. Liu, Phys. Plasmas **28**, 052905 (2021).
[30] T. D. Phan *et al.*, Nature (London) **557**, 202 (2018).
[31] P. Sharma Pyakurel *et al.*, Phys. Plasmas **26**, 82307 (2019).
[32] P. Shi, P. Srivastav, M. H. Barbhuiya, P. A. Cassak, E. E. Scime, and M. Swisdak, Phys. Rev. Lett. **128**, 025002 (2022).
[33] J. E. Stawarz *et al.*, Astrophys. J. **877**, L37 (2019).
[34] F. Califano, S. S. Cerri, M. Faganello, D. Laveder, M. Sisti, and M. W. Kunz, Front. Phys. **8**, 317 (2020).
[35] C. Vega, V. Roytershteyn, G. L. Delzanno, and S. Boldyrev, Astrophys. J. **893**, L10 (2020).
[36] N. F. Loureiro and S. Boldyrev, Astrophys. J. **890**, 55 (2020).
[37] I. Gingell *et al.*, Geophys. Res. Lett. **46**, 1177 (2019).
[38] N. Bessho, L.-J. Chen, S. Wang, M. Hesse, and L. B. Wilson III, Geophys. Res. Lett. **46**, 9352 (2019).
[39] R. Wang *et al.*, Geophys. Res. Lett. **45**, 4542 (2018).
[40] M. Hubbert, C. T. Russell, Y. Qi, S. Lu, J. L. Burch, B. L. Giles, and T. E. Moore, J. Geophys. Res. **127**, e2021JA029584 (2022).
[41] L. Franci, E. Papini, A. Micera, G. Lapenta, P. Hellinger, D. Del Sarto, D. Burgess, and S. Landi, Astrophys. J. **936**, 27 (2022).
[42] P. Shi *et al.*, Phys. Plasmas **28**, 032101 (2021).
[43] T. P. Intrator, X. Sun, G. Lapenta, L. Dorf, and I. Furno, Nat. Phys. **5**, 521 (2009).
[44] P. Shi, K. Huang, Q. Lu, and X. Sun, Plasma Phys. Contr. Fusion **61**, 125010 (2019).
[45] R. L. Stenzel and W. Gekelman, Phys. Rev. Lett. **42**, 1055 (1979).
[46] X. Sun, T. P. Intrator, L. Dorf, J. Sears, I. Furno, and G. Lapenta, Phys. Rev. Lett. **105**, 255001 (2010).
[47] B. Van Compernolle and W. Gekelman, Phys. Plasmas **19**, 102102 (2012).
[48] P. Shi *et al.*, Phys. Plasmas **29**, 032101 (2022).
[49] R. G. Kleva, J. F. Drake, and F. L. Waelbroeck, Phys. Plasmas **2**, 23 (1995).
[50] B. N. Rogers, R. E. Denton, J. F. Drake, and M. A. Shay, Phys. Rev. Lett. **87**, 195004 (2001).
[51] P. A. Cassak, J. F. Drake, and M. A. Shay, Phys. Plasmas **14**, 054502 (2007).
[52] J. Olson, J. Egedal, M. Clark, D. A. Endrizzi, S. Greess, A. Millet-Ayala, R. Myers, E. E. Peterson, J. Wallace, and C. B. Forest, J. Plasma Phys. **87**, 175870301 (2021).
[53] A. von Stechow, O. Grulke, and T. Klinger, Plasma Phys. Contr. Fusion **58**, 014016 (2016).
[54] J. Egedal, W. Fox, N. Katz, M. Porkolab, K. Reim, and E. Zhang, Phys. Rev. Lett. **98**, 015003 (2007).
[55] Y. Ren, M. Yamada, H. Ji, S. P. Gerhardt, and R. Kulsrud, Phys. Rev. Lett. **101**, 085003 (2008).
[56] Y. Ono, Y. Hayashi, T. Ii, H. Tanabe, S. Ito, A. Kuwahata, T. Ito, Y. Kamino, T. Yamada, and M. Inomoto, Phys. Plasmas **18**, 111213 (2011).
[57] P. Shi and E. E. Scime, Rev. Sci. Instrum. **94**, 023501 (2023).
[58] P. Shi, P. Srivastav, C. Beatty, R. S. Nirwan, and E. E. Scime, Rev. Sci. Instrum. **92**, 033102 (2021).
[59] See Supplemental Material at http://link.aps.org/supplemental/10.1103/PhysRevLett.131.155101 for a derivation of the parallel temperature, evidence that flux ropes are isotropic, a scaling analysis of betatron acceleration, the isotropization rate calculation, and details about the simulation. It includes Refs. [60–63].
[60] A. Zeiler, D. Biskamp, J. Drake, B. Rogers, M. Shay, and M. Scholer, J. Geophys. Res. **107**, 3783 (2002).
[61] C. K. Birdsall and A. B. Langdon, *Plasma Physics via Computer Simulation* (Taylor & Francis, London 2004).
[62] P. N. Guzdar, J. F. Drake, D. McCarthy, A. B. Hassam, and C. S. Liu, Phys. Fluids B **5**, 3712 (1993).
[63] U. Trottenberg, C. W. Oosterlee, and A. Schuller, *Multigrid* (Academic Press, San Diego, 2000).
[64] B. N. Rogers, R. E. Denton, and J. F. Drake, J. Geophys. Res. **108**, 1111 (2003).
[65] H. Arnold *et al.*, Phys. Rev. Lett. **126**, 135101 (2021).
[66] Y.-H. Liu, P. Cassak, X. Li, M. Hesse, S.-C. Lin, and K. Genestreti, Commun. Phys. **5**, 97 (2022).
[67] P. A. Cassak, Y.-H. Liu, and M. Shay, J. Plasma Phys. **83**, 715830501 (2017).
[68] L. Comisso and A. Bhattacharjee, J. Plasma Phys. **82**, 595820601 (2016).
[69] A. Bhattacharjee, Annu. Rev. Astron. Astrophys. **42**, 365 (2004).
[70] M. Inomoto *et al.*, Nucl. Fusion **59**, 086040 (2019).
[71] R. Numata and N. F. Loureiro, J. Plasma Phys. **81**, 305810201 (2015).

[72] J. V. Hollweg and H. J. Völk, J. Geophys. Res. **75**, 5297 (1970).
[73] Š. Štverák, P. Trávníček, M. Maksimovic, E. Marsch, A. N. Fazakerley, and E. E. Scime, J. Geophys. Res. **113**, A03103 (2008).
[74] A. Le, J. Egedal, O. Ohia, W. Daughton, H. Karimabadi, and V. S. Lukin, Phys. Rev. Lett. **110**, 135004 (2013).
[75] J. Egedal, A. Le, and W. Daughton, Phys. Plasmas **20**, 061201 (2013).
[76] A. Le, J. Egedal, W. Daughton, W. Fox, and N. Katz, Phys. Rev. Lett. **102**, 085001 (2009).
[77] A. S. Richardson, *2019 NRL Plasma Formulary* (US Naval Research Laboratory, Washington, DC, 2019), pp. 33–34.
[78] V. Roytershteyn, S. Dorfman, W. Daughton, H. Ji, M. Yamada, and H. Karimabadi, Phys. Plasmas **20**, 061212 (2013).
[79] J. P. Sauppe and W. Daughton, Phys. Plasmas **25**, 012901 (2018).
[80] S. Greess *et al.*, J. Geophys. Res. **126**, e2021JA029316 (2021).
[81] A. J. McCubbin, G. G. Howes, and J. M. TenBarge, Phys. Plasmas **29**, 052105 (2022).
[82] M. Yamada, J. Yoo, J. Jara-Almonte, H. Ji, R. M. Kulsrud, and C. E. Myers, Nat. Commun. **5**, 4774 (2014).
[83] R. L. Stenzel, W. Gekelman, and N. Wild, J. Geophys. Res. **87**, 111 (1982).
[84] J. R. Shuster, L.-J. Chen, W. S. Daughton, L. C. Lee, K. H. Lee, N. Bessho, R. B. Torbert, G. Li, and M. R. Argall, Geophys. Res. Lett. **41**, 5389 (2014).
[85] J. Egedal, B. Wetherton, W. Daughton, and A. Le, Phys. Plasmas **23**, 122904 (2016).
[86] H. Fu, E. E. Grigorenko, C. Gabrielse, C. Liu, S. Lu, K. J. Hwang, X. Zhou, Z. Wang, and F. Chen, Sci. China Earth Sci. **63**, 235 (2020).
[87] M. H. Barbhuiya, P. Cassak, M. Shay, V. Roytershteyn, M. Swisdak, A. Caspi, A. Runov, and H. Liang, J. Geophys. Res. **127**, e2022JA030610 (2022).